J|A|C|S
JOURNAL OF THE AMERICAN CHEMICAL SOCIETY

Unveiling Structure–Property Relationships in $Sr_2Fe_{1.5}Mo_{0.5}O_{6-\delta}$, an Electrode Material for Symmetric Solid Oxide Fuel Cells

Ana B. Muñoz-García,[†] Daniel E. Bugaris,[‡] Michele Pavone,[†,§] Jason P. Hodges,[∥] Ashfia Huq,[∥] Fanglin Chen,[⊥] Hans-Conrad zur Loye,[‡] and Emily A. Carter*[,†]

[†]Department of Mechanical and Aerospace Engineering, Program in Applied and Computational Mathematics, and Gerhard R. Andlinger Center for Energy and the Environment, Princeton University, Princeton, New Jersey 08544, United States

[‡]Department of Chemistry and Biochemistry, University of South Carolina, Columbia, South Carolina 29208, United States

[∥]Neutron Scattering Science Division, Oak Ridge National Laboratory, Oak Ridge, Tennessee 37831, United States

[⊥]Department of Mechanical Engineering, University of South Carolina, Columbia, South Carolina 29208, United States

Ⓢ *Supporting Information*

ABSTRACT: We characterize experimentally and theoretically the promising new solid oxide fuel cell electrode material $Sr_2Fe_{1.5}Mo_{0.5}O_{6-\delta}$ (SFMO). Rietveld refinement of powder neutron diffraction data has determined that the crystal structure of this material is distorted from the ideal cubic simple perovskite, instead belonging to the orthorhombic space group *Pnma*. The refinement revealed the presence of oxygen vacancies in the as-synthesized material, resulting in a composition of $Sr_2Fe_{1.5}Mo_{0.5}O_{5.90(2)}$ (δ = 0.10(2)). DFT+U theory predicts essentially the same concentration of oxygen vacancies. Theoretical analysis of the electronic structure allows us to elucidate the origin of this nonstoichiometry and the attendant mixed ion–electron conductor character so important for intermediate temperature fuel cell operation. The ease with which SFMO forms oxygen vacancies and allows for facile bulk oxide ion diffusivity is directly related to a strong hybridization of the Fe d and O p states, which is also responsible for its impressive electronic conductivity.

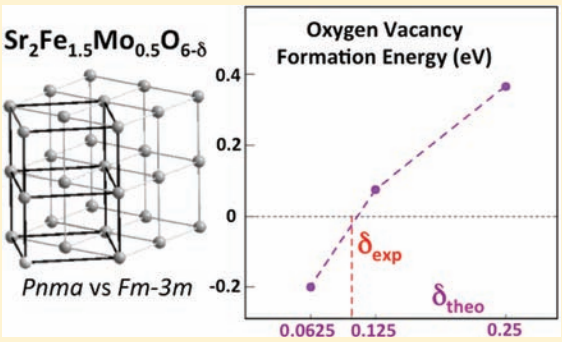

■ INTRODUCTION

Worldwide environmental concerns have been pushing the scientific community to develop new technologies for clean production of electricity. Fuel cell technology is one potentially very efficient and environmentally friendly way to convert the chemical energy of fuels into electricity, avoiding combustion processes with a high conversion rate. In particular, solid oxide fuel cells (SOFCs) can convert a wide variety of fuels with simpler and cheaper designs than those used in cells with liquid electrolytes, and SOFCs exhibit a lower sensitivity to fuel impurities.[1] Current research is focusing on the development of intermediate temperature (IT) SOFCs, which are meant to operate within the 500–800 °C range so as to diminish premature aging of the SOFC materials, thereby improving the durability, stability, and reliability of the devices.[2,3]

Recently, electrodes based on $Sr_2Fe_{1.5}Mo_{0.5}O_{6-\delta}$ (SFMO) were proven to be extremely efficient for IT-SOFCs.[4,5] In particular, SFMO has been used as both the cathode and anode material in a symmetrical configuration, demonstrating not only chemical compatibility with the electrolyte but also chemical stability in both reducing and oxidizing conditions, and remarkable electrocatalytic performance for both oxygen reduction and fuel oxidation.[6] SFMO exhibits the characteristic behavior of a mixed ionic and electronic conductor (MIEC), with good ionic and electrical conductivity. Its ionic conductivity is much higher than that of the commonly used cathode material $La_{0.8}Sr_{0.2}MnO_3$ and comparable to those of other cathode materials such as $La_{0.6}Sr_{0.4}CoO_3$ and $La_{0.6}Sr_{0.4}Co_{0.2}Fe_{0.8}O_3$.[4,7] SFMO also exhibits high electrical conductivity in both air and hydrogen environments, even comparable to that of Ni cermets.[6] Thus, SFMO-based SOFCs overcome the performance problems that appear when $LaMO_3$-based SOFCs run at ITs. These problems are related to slower electrode kinetics and interfacial polarization resistances, which are most pronounced at the cathode and thought to be related to the high polarization loss associated with the oxygen reduction reaction and the slow diffusion of oxide ions toward the electrolyte.[7,8]

A deep understanding of the reasons behind the success of SFMO for SOFC applications has been missing until now. Herein we report a joint experimental/theoretical characterization of the crystal and electronic structure of SFMO that reveals the subtle relationships between its structure and observed properties and performance. Our experimental characterization of SFMO highlights its inherent nonstoichio-

Received: February 3, 2012
Published: March 26, 2012

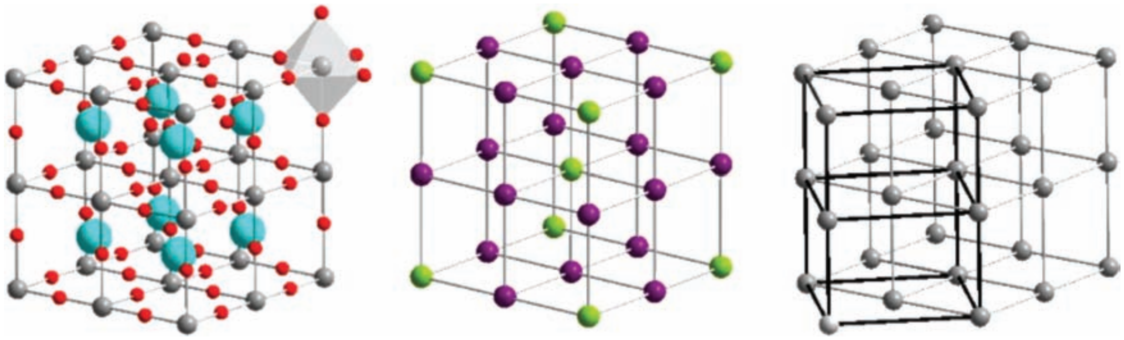

Figure 1. (Left) $Sr_8Fe_6Mo_2O_{24}$ cubic supercell of SFMO. Atom (color): Fe/Mo (gray), Sr (turquoise), O (red). (Middle) Isotropic distribution of Fe/Mo as studied in this work in the cubic SFMO supercell. Atom (color): Fe (purple), Mo (green). Sr and O atoms not shown for ease of viewing. (Right) Schematic of the pseudocubic cell (gray) arising from the *Pnma* cell (black) as studied in this work. The isotropic Fe/Mo distribution is used also in the calculations involving the pseudocubic cell.

metric nature, that is, oxygen vacancies naturally occur in the crystal structure; our first principle theoretical investigation explains why oxygen vacancies form so easily in this material. The presence of constitutional oxygen vacancies is key to understanding its effective action as an MIEC.

■ METHODS

SFMO was prepared by standard solid-state synthetic techniques. The starting reagents were $SrCO_3$ (Aldrich, 99.9+%), Fe_2O_3 (Alfa Aesar, 99.998%), and MoO_3 (Alfa Aesar, 99.95%). $SrCO_3$ was thoroughly dried overnight at ~150 °C to remove water; the other reagents were used as received. The first step was to synthesize $Fe_2Mo_3O_{12}$, with the purpose of sequestering the Mo in a ternary oxide and thereby preventing the loss of volatile MoO_3 during the prolonged high-temperature heating, as well as inhibiting the formation of $SrMoO_4$ from the direct reaction of $SrCO_3$ with MoO_3. To prepare $Fe_2Mo_3O_{12}$, a 1:3 stoichiometric ratio of Fe_2O_3 and MoO_3 was thoroughly ground with a mortar and pestle, before being placed in an alumina crucible. This mixture was placed in a furnace and heated at 12 °C/min up to 750 °C, whereupon it was held at that temperature for 12 h, followed by furnace cooling to room temperature. To confirm the phase purity of $Fe_2Mo_3O_{12}$, powder X-ray diffraction data were collected on a Rigaku Ultima IV powder diffractometer using Cu Kα radiation. Data were collected using the high-speed D/teX Ultra detector in 0.02° steps over the 2θ range 10−80° with a scan speed of 10°/min. All of the peaks in the powder pattern could be indexed in the monoclinic space group $P2_1$ with lattice parameters matching those reported in the literature for $Fe_2Mo_3O_{12}$.[9] In the next step of the synthesis of SFMO, a stoichiometric ratio of $SrCO_3$, Fe_2O_3, and $Fe_2Mo_3O_{12}$ was thoroughly ground with a mortar and pestle, before being placed in an alumina crucible. The reaction mixture was placed in a furnace and heated at 12 °C/min up to 1000 °C, held at this temperature for 12 h, and then furnace cooled to room temperature. The purpose of this step was to decompose the $SrCO_3$ to SrO and CO_2. The sample was then reground, placed in the alumina crucible, and heated in 5 h to 1200 °C, where the temperature was maintained for 12 h, before cooling to room temperature. This process was repeated 5 times, with intermittent grinding of the sample, and the collection of powder X-ray diffraction data to track the progress of the reaction. The reaction was deemed complete when the powder pattern of the SFMO sample no longer showed any change from the apparent cubic crystal system.

Time-of-flight (TOF) powder neutron diffraction data were collected on a 4.25 g sample of SFMO contained within a 6 mm diameter vanadium sample canister at 298 K. Diffraction profiles were collected using the POWGEN (BL-11A) neutron powder diffractometer at the Spallation Neutron Source at Oak Ridge National Laboratory, Oak Ridge, Tennessee.[10] Two different center wavelengths of 1.066 and 2.665 Å were used to collect data in the *d*-spacing ranges 0.32−3.2 and 1.7−8.3 Å, respectively. Rietveld refinement of the data was performed using the GSAS software package and the EXPGUI interface,[11,12] TOF peak-profile function number 3 (tabulated peak-shape dependency determined by use of NIST SRM-660b LaB_6 powder[10]) and the reciprocal interpolation function were used for modeling the diffraction peaks and background, respectively. The vanadium (sample canister) was refined as a second phase.

Spin-polarized density functional theory (DFT)[13] + U theory[14] was employed to overcome the large self-interaction error inherent in pure DFT when applied to mid-to-late first row transition metal oxides with tightly localized d-electrons.[15] The electron exchange-correlation functional used is the semilocal Perdew-Burke-Ernzerhof (PBE) version of the generalized gradient approximation[16] and the electron-ion interaction is handled by projector-augmented wave potentials.[17] All calculations were performed with the VASP 5.2 code.[18] We use a kinetic energy cutoff of 800 eV for the planewave basis and Brillouin zone sampling based on the Monkhorst-Pack (MP)[19] scheme. We use a 4×4×4/3×4×3/3×2×3 MP k-mesh in the 40/80/160-atom supercells (described below), respectively. These parameters ensured convergence of the computed total energy to within 1 meV per formula unit.

Frequently, the *U-J* parameter in DFT+U theory is tuned *ad hoc* to match a measured property of the system under study, rendering the method semiempirical. Here we choose the *U-J* value for Fe, $(U\text{-}J)_{Fe}$ = 4 eV, to be the average of those derived *ab initio* for FeO (*U-J* = 3.7 eV) and Fe_2O_3 (*U-J* = 4.3 eV),[20] appropriate for a mixed Fe(II)/Fe(III) material. This $(U\text{-}J)_{Fe}$ value, as well as the fact that no *U-J* is needed for Mo, was recently validated for the related Sr_2FeMoO_6 compound.[21] However, $Sr_2Fe_{1.5}Mo_{0.5}O_{6-\delta}$ also exhibits some Fe(IV) character (*vide infra*) and hence one may ask if a higher value of $(U\text{-}J)_{Fe}$, such as ~5 eV (derived assuming a linear increase in *U-J* with integer changes in oxidation state) might be warranted. As we shall show, the dominant Fe oxidation state of this Fe-rich material is Fe(III), suggesting a value ~4 eV is more appropriate. Nevertheless, test calculations utilizing $(U\text{-}J)_{Fe}$ = 5 eV and also with hybrid functionals incorporating exact exchange with no assumption of a particular *U-J* value (*vide infra*) show that our conclusions are robust with respect to our choice of $(U\text{-}J)_{Fe}$.

Our structural model of the SFMO material is based on a pseudocubic cell with 40 atoms ($Sr_8Fe_6Mo_2O_{24}$) that corresponds to a 2×2×2 supercell of the ideal cubic simple ABO_3 perovskite ($Pm\bar{3}m$) and could also represent a $\sqrt{2}\times1\times\sqrt{2}$ supercell of an orthorhombic distorted unit cell (*Pnma*). This model has the minimum size to study the Fe/Mo 3:1 ratio with different Fe/Mo atomic distributions. We use the isotropic distribution of Fe and Mo atoms (shown by Figure 1) to test the cubic vs orthorhombic cell structure. Because we find no significant differences between the two (*vide infra*), we impose cubic symmetry on the cell vectors and leave the ionic internal position free to relax with no symmetry constraint. In this way we can explore all the Fe/Mo relative distributions and several spin configurations within the same model with no fictitious distortions due to local aggregation of iron or molybdenum. We find the isotropic distribution of Fe/Mo

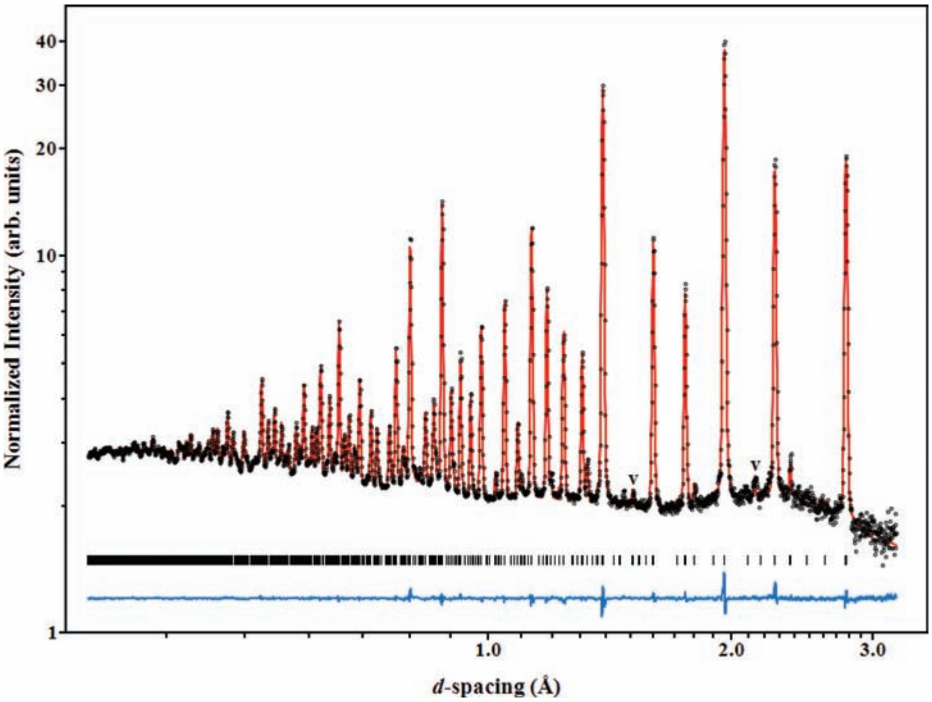

Figure 2. A log−log plot of the Rietveld refinement of powder neutron diffraction data for $Sr_2Fe_{1.5}Mo_{0.5}O_{6-\delta}$ (SFMO) at 298 K collected with a center wavelength of 1.066 Å. Open circles are observed data, the solid red line is the calculated pattern, and the blue line is the difference. Tick marks indicate the allowed Bragg reflections for SFMO. The small "v" marks two visible reflections from the vanadium sample canister (fitted as a second phase). R_p = 2.46%, R_{wp} = 3.76%, χ^2 = 12.48.

(with antiferromagnetic arrangements of Fe spins) to be the most stable; thus it is used subsequently to study oxygen vacancies. Removal of a neutral oxygen atom in the $Sr_8Fe_6Mo_2O_{24}$ cell leads to $Sr_2Fe_{1.5}Mo_{0.5}O_{6-\delta}$ with δ = 0.25. Both the ionic positions and the lattice constants are allowed to relax in both the stoichiometric and oxygen-deficient cells. We also explored smaller concentrations of oxygen vacancies, within $Sr_{16}Fe_{12}Mo_4O_{48}$ and $Sr_{32}Fe_{24}Mo_8O_{96}$ supercells, constructed as $\sqrt{2}\times\sqrt{2}\times1$ and $\sqrt{2}\times\sqrt{2}\times2$ supercells of the starting 40-atom cell. A single oxygen atom is removed from these cells, leading to δ = 0.125 and 0.0625, respectively. The oxygen vacancy formation energy ($E_{\text{form}}O^*$) is computed from the energies of the systems with (defect) and without (host) the oxygen vacancy and is referenced to the gaseous oxygen molecule in its triplet ground state calculated at the same level of theory [$E_{\text{form}}O^* = E_{\text{defect}} - E_{\text{host}} + 1/2\ O_2(g)$].

These computed values correspond to the enthalpy of the formation of the defect; for simplicity we neglect finite temperature entropic contributions due to lattice and O_2 vibrations (and O_2 rotations and translations) as well as configurational entropy. These effects are mostly relevant at high temperature, for example, for modeling SOFC operating conditions whereas here we study the intrinsic properties of the SFMO materials at room temperature, where entropic effects are not expected to dominate. As the temperature rises, configurational entropy will play an increasingly important role, and will merely lower the free energy of formation of vacancies even more than what is reported below. Atom- and angular momentum-projected densities of states (PDOS) and magnetic moments were obtained as direct output of the VASP code. Topological analysis of the electron density was carried out employing the Bader approach.[22] Further computational details are provided in the Supporting Information section.

■ RESULTS AND DISCUSSION

On the basis of a Rietveld refinement of powder X-ray diffraction data, $Sr_2Fe_{1.5}Mo_{0.5}O_6$ was initially reported to crystallize as a cubic double perovskite in space group $Fm\overline{3}m$ with lattice parameter a = 7.8717(1) Å.[23] In the cubic double perovskite, $A_2BB'O_6$, the oxygen is shifted slightly off the special position and occupies the *e* Wyckoff position of the $Fm\overline{3}m$ group ((*x*,0,0), $x \neq 0.25$), which results in two nonequivalent metal sites, B and B′. However, according to the refinement, the value of the *x*-coordinate for O was shifted very minimally (x = 0.2590(11)), and the occupancies of the B and B′ sites retained essentially the 3:1 ratio of Fe to Mo indicated by the empirical formula. As such, there was no apparent ordering of the metals on the B and B′ sites. Therefore, a subsequent report in the literature proposed a simple cubic perovskite structure for $Sr_2Fe_{1.5}Mo_{0.5}O_{6-\delta}$, again on the basis of a Rietveld refinement of powder X-ray diffraction data.[5] The space group was given as $Pm\overline{3}m$ with lattice parameter a = 3.92874(6) Å. In the simple cubic perovskite structure, ABO_3, the oxygen atom is located on a special position midway between two crystallographically equivalent B metal sites. Oxygen atoms occupy the *d* Wyckoff positions within the $Pm\overline{3}m$ group with coordinates (0.5, 0, 0). In the $Pm\overline{3}m$ 2×2×2 supercell, which is comparable to the cubic double perovskite structure, this would correspond to oxygen atoms placed at (0.25, 0, 0). The authors of the first report specified a fully oxidized formula of $Sr_2Fe_{1.5}Mo_{0.5}O_6$, despite the material being sintered in 5% H_2/Ar, whereas the authors of the second report suggested an oxygen-deficient material with formula $Sr_2Fe_{1.5}Mo_{0.5}O_{6-\delta}$. We expect that the structure of this material is very sensitive to the concentration of oxygen vacancies, which in turn depends highly on the preparative conditions, particularly the rate of cooling.

According to the Rietveld refinement of our current powder neutron diffraction data (Figure 2), SFMO is only pseudocubic, instead belonging to space group *Pnma* of the orthorhombic system. Initial refinements were performed in the cubic space groups $Fm\overline{3}m$ and $Pm\overline{3}m$. Although the highest intensity peaks can be fit well to the listed cubic space groups, the refinements failed to adequately account for many weak superstructure peaks. Therefore, it became necessary to investigate a number of distorted perovskite tilt systems in lower symmetry space groups.[24]

The Structure Prediction Diagnostic Software[25] suggested the following space groups, along with tilt systems and global instability index values (where the lowest value is the most stable structure): $Pm\bar{3}m$ ($a^0a^0a^0$; 0.1585), $I4/mcm$ ($a^0a^0c^-$; 0.26227), $P4/mbm$ ($a^0a^0c^-$; 0.2788), $I4/mmm$ ($a^0b^+b^+$; 0.3156), $R\bar{3}c$ ($a^-a^-a^-$; 0.26174), and $Pnma$ ($a^-b^+a^-$; 0.16229). As mentioned above, the refinement in $Pm\bar{3}m$ did not sufficiently model a number of weak superstructure peaks despite a satisfactory convergence. The refinements in space groups $I4/mcm$, $P4/mbm$, and $I4/mmm$ all failed to converge. This left space groups $R\bar{3}c$ and $Pnma$ as possible options in the refinement of the powder neutron diffraction data for SFMO. For both space groups, the refinements fully converged, though better agreement was found for the refinement in $Pnma$ (R_p = 2.46%, R_{wp} = 3.76%, χ^2 = 12.48) than the one in $R\bar{3}c$ (R_p = 2.63%, R_{wp} = 3.81%, χ^2 = 14.28). Additionally, examining the refinement in $R\bar{3}c$, the positions of the superstructure peaks are displaced from the observed peaks, suggesting that the structure is not rhombohedrally distorted. Both the positions and intensities of the superstructure peaks are well accounted for in the refinement in $Pnma$, indicating that this is the correct space group for SFMO. It should not be surprising that SFMO assumes this space group, as it is the most common (along with the nonstandard setting $Pbnm$) among the simple perovskites.[25] This structure type is commonly referred to as the $GdFeO_3$ structure type,[26] with some other examples including Sr_2FeMO_6 (M = Nb, Ta),[27] $SrLaFeSnO_6$,[28] $CaMoO_3$,[29] $Ca(M_{0.5}Mo_{0.5})O_3$ (M = V, Cr),[30] and $SrLaCr_{1.5}Mo_{0.5}O_6$.[31]

The $Pnma$ space group has only one B metal site, making it a simple perovskite (ABO_3) so that SFMO can be written as $Sr_2Fe_{1.5}Mo_{0.5}O_{6-\delta}$, or more formally as $Sr(Fe_{0.75}Mo_{0.25})O_{3-(\delta/2)}$. The lattice parameters in orthorhombic space group $Pnma$ can be related to the lattice parameter of the ideal simple cubic perovskite in $Pm\bar{3}m$ (a_0) according to the relationships $a \approx b \approx \sqrt{2}a_0$, $c \approx 2a_0$. The structural difference between the orthorhombic and cubic perovskites is in this case due to the tilting of the MO_6 (M = Fe or Mo) octahedra. The reason for this distortion is that the Sr^{2+} cation is too small to accommodate the corner-sharing MO_6 octahedral network in a true cubic perovskite. The tilting of the MO_6 octahedra shortens the Sr−O bond distances (more favorable energetically), while maintaining the same first coordination sphere around the M cation.

The lattice parameters and Fe/Mo−O bond distances for SFMO, as well as the atomic positions are given in Tables 1 and 2. Refinement of the Fe and Mo occupancies did not deviate from the expected ratio by more than one standard deviation (confirming that there are no cationic vacancies), therefore they were fixed at the ideal 3:1 ratio dictated by the solid-state synthetic procedure. When refining the site occupancies of the oxygen atoms, it was determined that O(2) is fully occupied, but O(1) exhibits vacancies. The site occupancy of O(1) was refined to a value of 0.976(6), resulting in a δ of 0.10(2), and an empirical formula of $Sr_2Fe_{1.5}Mo_{0.5}O_{5.90(2)}$ for the as-synthesized SFMO. It is notable that this phase, prepared in air, possesses inherent oxygen vacancies in its crystal structure. This feature will aid in the explanation of the transport properties of SFMO (*vide infra*).

Table 1. Structural Refinement Results for SFMO from Powder Neutron Diffraction

space group	*Pnma*
δ	0.10(2)
a (Å)	5.5420(5)
b (Å)	7.8270(4)
c (Å)	5.5472(6)
Fe/Mo−O(2) × 2 (Å)	1.953(5)
Fe/Mo−O(1) × 2 (Å)	1.9640(3)
Fe/Mo−O(2) × 2 (Å)	1.969(5)
average Fe/Mo−O (Å)	1.962(2)

Our *ab initio* DFT+U calculations find the $Fm\bar{3}m$ and the $Pnma$ structures to be essentially degenerate (the respective total energies differ by ~0.2 meV/f.u.). The orthorhombic cell is slightly lower in energy, in agreement with experiment. The lattice parameters of these two cells are given in Table 3. In the orthorhombic case, the predicted a:b:c ratio is 1:1.41339:1.00036, which means a cell slightly closer to cubicity than the experimental one (ratio 1:1.41231:1.0094), and the lattice constants are at most 1.1% larger than the experimental ones. In the cubic case, the predicted lattice constant is 0.6% larger than reported in ref 23. The small overestimation of computed cell volume and interatomic distances is an expected shortcoming of the DFT-PBE+U method as well as of the higher oxygen content of the stoichiometric material. When oxygen vacancies are introduced at concentrations similar to the experiment, the lattice parameters decrease slightly (<1%), as expected, rendering the agreement between theory and experiment even better. The negligible difference in terms of absolute energies between the orthorhombic ($Pnma$) and the cubic ($Fm\bar{3}m$) cells is also reflected in the oxygen vacancy formation energy. The $E_{\text{form}}O^*$ in SFMO (δ = 0.25), calculated in the $Pnma$ and $Fm\bar{3}m$ cells, differ by less than 0.2 meV. These results, together with the fact that structural transitions from orthorhombic to cubic symmetry have been reported for a variety of perovskites at SOFC operating temperatures,[32] make the $Fm\bar{3}m$ cubic cell an excellent model for the qualitative and quantitative simulation of oxygen vacancies and electronic properties in SFMO. Thus, in what follows, all subsequent theoretical predictions are derived from calculations performed on the cubic cell.

By removing one neutral oxygen atom from $Sr_8Fe_6Mo_2O_{24}$, $Sr_{16}Fe_{12}Mo_4O_{48}$, and $Sr_{32}Fe_{24}Mo_8O_{96}$ supercells, we explored theoretically $Sr_2Fe_{1.5}Mo_{0.5}O_{6-\delta}$ lattices with oxygen vacancy concentrations of δ = 0.25, 0.125, and 0.0625. These concentrations bracket the average experimental value of δ = 0.10(2). We considered the two different oxygen vacancies that can be formed in this material with an isotropic distribution of Fe and Mo: those between two Fe ions (Fe−O*−Fe) and those between a Mo and a Fe ion (Mo−O*−Fe).

The calculated average values of $E_{\text{form}}O^*$ and the range obtained for the different spin configurations studied (see Supporting Information) are shown in Figure 3. We predict E_{form}(Mo−O*−Fe) to be higher than E_{form}(Fe−O*−Fe) at all vacancy concentrations considered. The main reason that Fe−O*−Fe vacancies are much more favorable than Mo−O*−Fe ones is because mid-to-late transition metals such as Fe form much weaker metal−oxygen bonds than early transition metals such as Mo.[33,34] Therefore Fe−O bonds are easier to break in order to remove oxygen from the lattice to form a vacancy. We had similarly predicted that the related material Sr_2FeMoO_6 preferentially forms vacancies along Fe−O−Fe bonds rather than along Mo−O−Fe and Mo−O−Mo bonds.[21] Most

Table 2. Atomic Parameters for SFMO from the Rietveld Refinement of Powder Neutron Diffraction Data

	x	y	z	U_{iso}	occupancy
Sr	0.0013(4)	0.25	0.504(1)	0.0104(2)	1.0
Fe	0	0	0	0.00570(9)	0.75
Mo	0	0	0	0.00570(9)	0.25
O(1)	0.0168(6)	0.25	0.0254(5)	0.0082(5)	0.976(6)
O(2)	0.2550(8)	0.5032(9)	0.2429(7)	0.0123(3)	1.0

Table 3. Calculated (DFT+U) Structural Parameters for SFMO[a]

space group	$Fm\bar{3}m$	$Fm\bar{3}m$	$Fm\bar{3}m$	$Fm\bar{3}m$	$Pnma$	$Pnma$
δ	0	0.0625	0.125	0.25	0	0.25
a (Å)	7.919(4)	7.896(1)	7.893(1)	7.892(2)	5.600(0)	5.572(1)
b (Å)	–	–	–	–	7.915(2)	7.853(9)
c (Å)	–	–	–	–	5.602(2)	5.590(2)
Mo–O (Å)	1.928(9)	1.926(5)	1.920(8)	1.918(4)	1.928(9)	1.921(1)
Fe–O–(Mo) (Å)	2.030(7)	2.030(1)	2.028(1)	2.026(0)	2.029(7)	2.027(0)
Fe–O–(Fe) (Å)	1.945(6)	1.941(7)	1.939(2)	1.932(3)	1.938(7)	1.930(8)
	2.014(1)	2.013(6)	2.008(3)	2.002(5)	2.019(5)	2.009(3)
Fe–Fe (Å)	3.959(7)	3.948(1)	3.946(6)	3.946(3)	3.958(7)	3.941(7)
Fe–Mo (Å)	3.959(7)	3.948(0)	3.946(5)	3.946(1)	3.959(4)	3.940(5)

[a] Calculated lattice constants, M–O and M–M distances for the cubic stoichiometric material ($Fm\bar{3}m$, $\delta = 0$) are the average of all obtained for all the spin arrangements within the Fe sublattice studied; those reported for non-stoichiometric SFMO (δ = 0.0625, 0.125, 0.25) correspond to the lowest-energy spin arrangement.

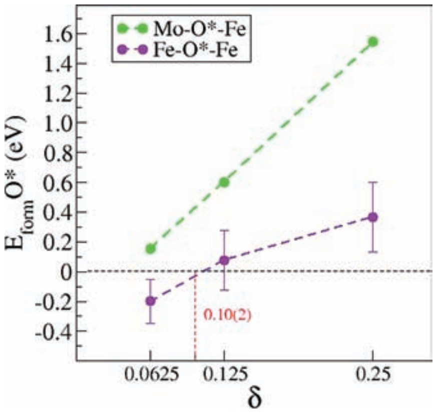

Figure 3. Calculated (DFT+U) formation energies of an oxygen vacancy (E_{form}O*) along Mo–O–Fe and Fe–O–Fe bonds from the $Sr_8Fe_6Mo_2O_{24}$, $Sr_{16}Fe_{12}Mo_4O_{48}$, and $Sr_{32}Fe_{24}Mo_8O_{96}$ cells, corresponding to δ values in $Sr_2Fe_{1.5}Mo_{0.5}O_{6-\delta}$ equal to 0.25, 0.125 and 0.0625, respectively. Ranges obtained from different spin configurations (see Supporting Information) are shown between bars; the average value is represented by a dot. The black dashed line demarcates zero energy and the red dashed line designates the experimental δ.

importantly, we predict average oxygen vacancy formation energies (Fe–O*–Fe) near zero for the more realistic concentrations explored, in complete agreement with the inherent nonstoichiometry of Fe-rich SFMO that is observed experimentally. Lastly, we confirmed the quality of our DFT+U predictions by performing single-structure total energy calculations using the HSE hybrid exchange-correlation functional that contains exact exchange in a less approximate though very expensive fashion.[35] DFT+U and DFT-HSE (using DFT+U structures) oxygen vacancy formation energies and electronic features are in quantitative and qualitative agreement, with details reported in the Supporting Information.

Our theoretical results also explain the tendency of the material to exhibit vacancies preferentially on the O(1) sites. As mentioned above, given that no aggregation of Mo is observed in this material, the two main M–O–M bonds found in SFMO are Mo–O–Fe and Fe–O–Fe bonds. The calculated M–O and M–M distances along these bonds are given in Table 3. As expected for a pseudocubic system, the Fe–Fe distance along an Fe–O–Fe bond is nearly the same as the Mo–Fe distance along a Mo–O–Fe bond. In the Mo–O–Fe moieties, the shortest metal–oxygen bond is predicted to be the Mo–O one, as expected from the fact that the Mo–O bond is stronger. Accordingly, the Fe–O bonds along Mo–O–Fe moieties are larger. By contrast, the position of the oxygen atom between two Fe ions is more symmetric, thereby producing two Fe–O bond lengths along a Fe–O–Fe bond intermediate between those along Mo–O–Fe. This analysis, together with the data in Table 1 showing two nonequivalent bond lengths involving O(2), suggests that the O(2) position detected experimentally comes from oxygen atoms mostly involved in Fe–O–Mo bonds. The O(1) atoms, those prone to form the vacancies according to the Rietveld refinement, would then be mostly the Fe–O(1)–Fe ones, which are, precisely, the ones predicted by our calculations to spontaneously form an oxygen vacancy due to the weaker Fe–O bonds.

Facile vacancy formation has important implications for ion transport. Because it is well known that in perovskite-type transition metal oxides the diffusion of oxygen anions occurs through a vacancy hopping mechanism,[36] the presence of an elevated concentration of oxygen vacancies is directly responsible for this material's high ionic conductivity. The measured activation energy in the case of vacancy hopping is the sum of the vacancy formation energy and the migration energy (the energy for the oxide ion to hop from one site to a vacant neighboring site). With the vacancy formation energy predicted to be near zero in SFMO (as opposed to the more typical several eV[37,38]), the overall activation energy is reduced dramatically, facilitating oxide ion diffusion, as observed.[4]

The formation of an oxygen vacancy can be viewed as a process of breaking metal-oxo bonds followed by the removal of a neutral oxygen atom and the subsequent redistribution of the extra electrons from the oxide ion into the SFMO lattice. To further clarify the origin of the inherent presence of oxygen vacancies in SFMO, we analyzed its electron density by computing effective Bader charges[22] of SFMO atoms before and after the vacancy is formed, which yields a qualitative picture of the reorganization of the electron density upon removal of a neutral oxygen atom. Fe atoms in the stoichiometric material carry a charge between +1.63*e* and +1.73*e*, Mo atoms +2.37*e*, Sr ions +1.61*e*, and oxygen atom charges range between −1.12*e* and −1.17*e*. We find these same values in all three $Sr_8Fe_6Mo_2O_{24}$, $Sr_{16}Fe_{12}Mo_4O_{48}$, and $Sr_{32}Fe_{24}Mo_8O_{96}$ supercells, regardless of the spin distributions within the Fe sublattice. These Bader charges indicate significant covalent character is present in the Fe−O and Mo−O bonds (since in this material without vacancies Fe and Mo have formal oxidation states of +3 to +4 and +5 to +6, respectively). However, both Fe and Mo Bader charges are higher than those reported for Sr_2FeMoO_6 that exhibits mixed $Fe^{(3-\delta)+}$ and $Mo^{(5+\delta)+}$ oxidation states, suggesting that $SrFe_{1.5}Mo_{0.5}O_6$ has higher oxidation states of $Fe^{(3+\delta)+}$ and Mo^{6+}. By contrast, Sr ions mostly interact through ionic bonding (with a Bader charge close to its formal charge of +2) with the rest of the lattice. These findings are in agreement with previous XPS analysis showing that Fe^{3+} and Mo^{6+} species dominate at room temperature.[5] Assuming Mo^{6+} and $\delta \approx 0.1$, the average charge on Fe is +3.2. In other words, SFMO is expected to have the following composition: $Sr(+2)_2Fe(+3)_{1.2}Fe(+4)_{0.3}Mo(+6)_{0.5}O(-2)_{5.9.}$

After the Fe−O*−Fe vacancy is created, Bader analysis of the $Sr_8Fe_6Mo_2O_{23}$, $Sr_{16}Fe_{12}Mo_4O_{43}$ and $Sr_{32}Fe_{24}Mo_8O_{95}$ cells reveals a high degree of delocalization of the extra charge (∼−1.12/−1.17*e*) left behind by the departing oxygen. We find that the oxygen vacancy formation energy decreases with increasing ability of the material to spread out the extra charge left behind by the removed oxygen atoms. In the smaller cell, ∼−1.00*e* is mainly distributed among the nine oxygen atoms directly linked to the cations adjacent to the oxygen vacancy. In the larger cells, which model a more realistic concentration of oxygen vacancies, ∼−1.00*e* of extra charge is fully delocalized among all the oxygen atoms in the cell. Cations are much less involved in the delocalization of the charge: only a residual −0.12/−0.17*e* appears to be distributed among all the Fe ions in the cell. Consistent with this finding, previous work on Sr_2FeMoO_6 and ABO_3 perovskites correlated large oxygen vacancy formation energies with high degrees of localization of the charge.[21,37a]

The electron delocalization upon oxygen vacancy formation is the key feature responsible for the very low vacancy formation energy. Although the oxidation state of the cations does affect the electronic structure upon the oxygen vacancy formation, it is not the controlling factor in these materials. By contrast, in the related material $LaFeO_3$ (LFO), formation of an oxygen vacancy leads to the localized reduction of the two next-nearest-neighbor ions from $Fe^{3+}(d^5)$ to $Fe^{2+}(d^6)$.[37a] We were actually expecting a similar and even more favorable "local" reduction process in SFMO, because of the $Fe^{3+/4+}$ mixed valence, but instead we found electron delocalization onto the oxygen sublattice. The main difference between LFO and SFMO is not the oxidation state of iron, but rather the nature of the Fe−O bond. Bader charge analysis can help to quantify the ionicity vs covalency of a bond: the closer the Bader charge is to the formal oxidation state the more ionic is the bond. Fe and O in LFO have Bader charges of +1.71 and −1.26, respectively. The same ions in stoichiometric SFMO have Bader charges of +1.63 and −1.17. The Fe−O bond is thus slightly more covalent in SFMO than in LFO and therefore it is possible to add more negative charge to the O sublattice (since it is not already saturated with electrons). This subtle change in covalency is the key to understanding the delocalization of extra charge onto the oxygen sublattice.

SFMO's ability to delocalize the extra charge upon oxygen vacancy formation is directly related to the electronic features of this material. Figure 4 displays the PDOS for SFMO supercells with δ = 0 and 0.125. We observe analogous PDOS vs E patterns for all cell sizes and spin configurations studied. For defect-free SFMO, we predict that p states of oxygen and d states of iron strongly hybridize and cross the Fermi level. The formation of oxygen vacancies (at realistic concentrations) does not jeopardize the hybridization of the Fe and O states and the availability of empty states at the edge of the conduction band (Figure 4 bottom panel). These features are consistent with the

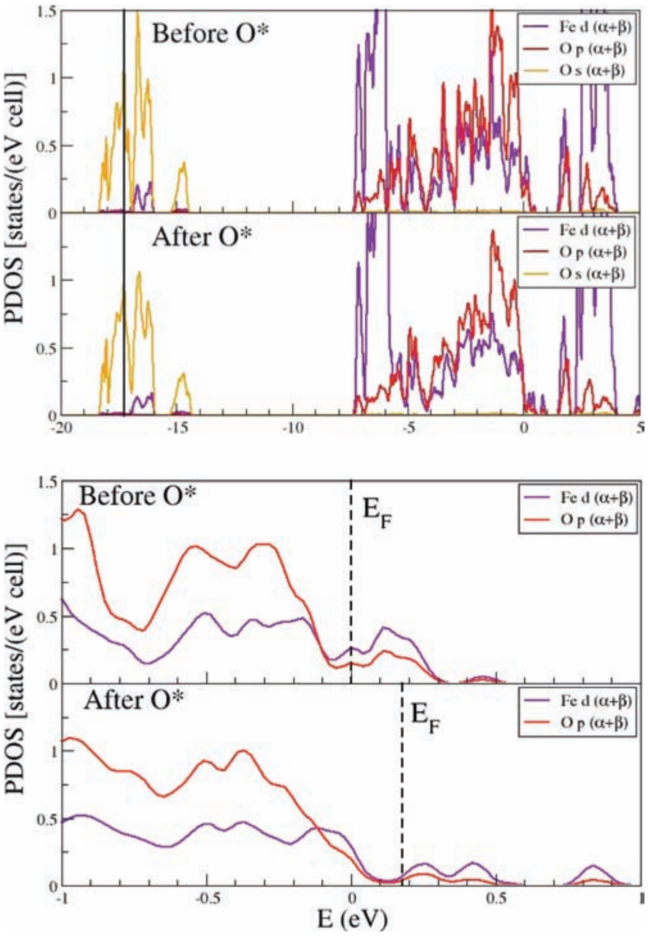

Figure 4. (Top) Projected densities of states (PDOS) of $Sr_2Fe_{1.5}Mo_{0.5}O_{6-\delta}$ (δ = 0.0 and δ = 0.125, with an Fe−O*−Fe vacancy) at the DFT+U level of theory with $(U\text{-}J)_{Fe}$ = 4 eV. Sums of α- and β-spin PDOS on Fe(d), Mo(d) and O(p) orbitals are shown. (Bottom) Zoom-in near the Fermi level. The band energies are shifted such that the Fermi energy (E_F) is set to zero for the stoichiometric material (δ = 0). Then the energy scale for the nonstoichiometric material is adjusted to align its O 2s states with the δ = 0 case (solid vertical line). Dashed lines indicate the relevant Fermi energies. Mo PDOS are not shown for ease of viewing, since they are negligible near the Fermi level.

high electronic conductivity found in SFMO and other Fe-rich perovskites,[39−41] which has been proposed to be due to percolation paths for the electrons to move through the crystal comprised exclusively of Fe−O−Fe bonds.[40] As pointed out by Tuller,[42] the 3d$_{e_g}$ orbitals of iron cations may overlap with the 2p$_\sigma$ orbitals of O^{2-} ions to form σ-bonds (e$_g$−p$_\sigma$−e$_g$ bonds) and the 3d$_{t_{2g}}$ orbitals of iron ions may overlap with the 2p$_\pi$ of O^{2-} ions to form π-bonds (t$_{2g}$−p$_\pi$−t$_{2g}$ bonds). The remarkably high experimental values of charge transport within the SFMO electrodes (p-type at the cathode/n-type at the anode) therefore are likely due to the observed strong hybridization of the Fe and O states at the conduction band edge. Such a band is not fully populated and has empty states just above the Fermi level, thus implying a high mobility of electrons/holes along the Fe−O−Fe bonding network. Therefore, the excess electron density left by the formation of the vacancy can easily occupy these empty states across the Fermi level, thus leading to the observed charge delocalization discussed above. In general terms, the effect of oxygen vacancies on the electron conductivity is small as long as the concentration of vacancies is small enough to prevent interruption of the three-dimensional hopping/percolation path through nondefective Fe−O−Fe links.

■ CONCLUSIONS

In summary, key properties of the very promising, recently proposed SFMO symmetric fuel cell electrode material were characterized by means of a joint experimental and theoretical effort. Powder neutron diffraction was instrumental for assigning unambiguously the orthorhombic space group *Pnma* to the SFMO crystal structure. The oxygen nonstoichiometry found by experiment agrees remarkably well with the *near zero* oxygen vacancy formation energy computed from first-principles quantum mechanics. Such a high concentration of constitutional oxygen vacancies is very likely responsible for boosting oxide ion bulk diffusion. Beyond understanding the thermodynamic reasons behind the observed oxygen non-stoichiometry, our theoretical work provides analysis of the SFMO electronic structure. The very low oxygen vacancy formation energy has two origins: (1) relatively weak Fe−O bonds and (2) a fully delocalized rearrangement of the extra charge delivered to the lattice upon removal of the neutral oxygen atom, in contrast to simple perovskite materials. The strong hybridization of Fe d- and O p-states plays a crucial role in such behavior. Additionally, empty states across the Fermi energy in the SFMO conduction band are still retained at the experimental vacancy concentration, which is undoubtedly responsible for the high electronic conductivity of this material. Thus the combination of facile vacancy formation, leading to sufficiently high oxide ion bulk diffusivity—while retaining metallic character—leading to adequate electronic conductivity, provides the reasons why this material functions so well as an MIEC. Lastly, these findings suggest a new design principle to use in the search for IT-SOFC materials: use of perovskites enriched with late transition metals to weaken the transition metal-oxo bonds and to enhance metal d−O p hybridization so that the reduced material delocalizes the extra charge left behind so as to retain metallic character.

■ ASSOCIATED CONTENT

Ⓢ Supporting Information

Standard plots of the Rietveld refinement of powder neutron diffraction data for $Sr_2Fe_{1.5}Mo_{0.5}O_{6-\delta}$ (SFMO) at 298 K collected with center wavelengths of 1.066 and 2.665 Å, representation of the different Fe/Mo atomic and spin configurations with their corresponding Fe−O*−Fe and Mo−O*−Fe oxygen vacancies as studied in this work and a table comparing formation energies of oxygen vacancies, Fe magnetic moments, and changes in Bader charges for the PBE +U (U-J_{Fe} = 4) and HSE methods. This material is available free of charge via the Internet at http://pubs.acs.org.

■ AUTHOR INFORMATION

Corresponding Author

eac@princeton.edu

Notes

The authors declare no competing financial interest.

[§] Permanent address for M.P.: Department of Chemistry, University of Napoli Federico II, Napoli 80120, Italy

■ ACKNOWLEDGMENTS

This work was supported as part of HeteroFoaM, an Energy Frontier Research Center funded by the U.S. Department of Energy, Office of Science, and Office of Basic Energy Sciences under Award Number DE-SC0001061. Use of the Spallation Neutron Source is supported by the Division of Scientific User Facilities, Office of Basic Energy Sciences, U.S. Department of Energy, under contract DE-AC05-00OR22725 with UT-Battelle, LLC.

■ REFERENCES

(1) (a) Park, S.; Vohs, J. M.; Gorte, R. J. *Nature* **2000**, *404*, 265. (b) Boudghene-Stambouli, A.; Traversa, E. *Renew. Sust. Energy Rev.* **2002**, *6*, 433. (c) Wachsman, E. D.; Singhal, S. C. *Am. Ceram. Soc. Bull.* **2010**, *89*, 23.

(2) (a) Steele, B. C. H.; Heinzel, A. *Nature* **2001**, *414*, 345. (b) Ruiz-Morales, J. C.; Marrero, D.; Savaniud, C.; Savvin, S. N. *Energy Environ. Sci.* **2010**, *3*, 1670. (c) Yang, L.; Wang, S.; Blinn, K.; Liu, M.; Cheng, Z.; Liu, M. *Science* **2009**, *326*, 126.

(3) (a) Jacobson, A. J. *Chem. Mater.* **2010**, *22*, 660. (b) Orera, A.; Slater, P. R. *Chem. Mater.* **2010**, *22*, 675.

(4) Xiao, G.; Liu, Q.; Zhao, F.; Zhang, L.; Xia, C.; Chen, F. *J. Electrochem. Soc.* **2011**, *158*, B455.

(5) Liu, Q.; Bugaris, D. E.; Xiao, G.; Chmara, M.; Ma, S.; zur Loye, H.-C.; Amiridis, M. D.; Chen, F. *J. Power Sources* **2011**, *196*, 9148.

(6) Liu, Q.; Dong, X.; Xiao, G.; Ma, S.; Zhao, F.; Chen, F. *Adv. Mater.* **2010**, *22*, 5478.

(7) Sun, C.; Hui, R.; Roller, J. *J. Solid State Electrochem.* **2010**, *14*, 1125.

(8) Adler, S. B. *Chem. Rev.* **2004**, *104*, 4791.

(9) Rapposch, M. H.; Anderson, J. B.; Kostiner, E. *Inorg. Chem.* **1980**, *19*, 3531.

(10) Huq, A.; Hodges, J. P.; Gourdon, O.; Heroux, L. *Z. Kristallogr. Proc.* **2011**, *1*, 127.

(11) Larson, A. C.; von Dreele, R. B. *General Structure Analysis System (GSAS)*; Los Alamos National Laboratory: Los Alamos, NM, 1990.

(12) Toby, B. H. *J. Appl. Crystallogr.* **2001**, *34*, 210.

(13) (a) Hohenberg, P.; Kohn, W. *Phys. Rev.* **1964**, *136*, B864. (b) Kohn, W.; Sham, L. J. *Phys. Rev.* **1965**, *140*, A1133.

(14) (a) Anisimov, V. I.; Zaanen, J.; Andersen, O. K. *Phys. Rev. B* **1991**, *44*, 943. (b) Anisimov, V. I.; Aryasetiawan, F.; Lichtenstein, A. *J. Phys.: Condens. Matter* **1997**, *9*, 767.

(15) (a) Carter, E. A. *Science* **2008**, *321*, 800. (b) Huang, P.; Carter, E. A. *Annu. Rev. Phys. Chem.* **2008**, *59*, 261.

(16) Perdew, J. P.; Burke, K.; Ernzerhof, M. *Phys. Rev. Lett.* **1996**, *77*, 3865.

(17) (a) Blöchl, P. *Phys. Rev. B* **1994**, *50*, 17953. (b) Kresse, G; Joubert, D. *Phys. Rev. B* **1999**, *59*, 1758.

(18) (a) Kresse, G.; Hafner, J. *Phys. Rev. B* **1993**, *48*, 13115. (b) Kresse, G; Furthmüller, J. *Phys. Rev. B* **1996**, *54*, 11169. (c) Kresse, G.; Furthmüller, J. *Comput. Mater. Sci.* **1996**, *6*, 15.

(19) Monkhorst, H. J.; Pack, J. D. *Phys. Rev. B* **1976**, *13*, 5188.

(20) (a) Mosey, N. J.; Liao, P.; Carter, E. A. *J. Chem. Phys.* **2008**, *129*, 14103. (b) Mosey, N. J.; Carter, E. A. *Phys. Rev. B* **2006**, *76*, 155123.

(21) Muñoz-Garcia, A. B.; Pavone, M.; Carter, E. A. *Chem. Mater.* **2011**, *23*, 4525.

(22) (a) Bader, R. F. W. *Atoms in Molecules - A quantum theory*; Oxford University Press: New York, 1990. (b) Tang, W.; Sanville, E.; Henkelman, G. *J. Phys.: Condens. Matter* **2009**, *21*, 084204.

(23) Liu, G. Y.; Rao, G. H.; Feng, X. M.; Yang, H. F.; Ouyang, Z. W.; Liu, W. F.; Liang, J. K. *J. Alloys Comp.* **2003**, *353*, 42.

(24) (a) Woodward, P. *Acta Crystallogr., Sect. B: Struct. Sci.* **1997**, *53*, 32. (b) Woodward, P. *Acta Crystallogr., Sect. B: Struct. Sci.* **1997**, *53*, 44.

(25) Lufaso, M. W.; Woodward, P. M. *Acta Crystallogr., Sect. B: Struct. Sci.* **2001**, *57*, 725.

(26) Geller, S. *J. Chem. Phys.* **1956**, *24*, 1236.

(27) (a) Tezuka, K.; Henmi, K.; Hinatsu, Y.; Masaki, N. M. *J. Solid State Chem.* **2000**, *154*, 591. (b) Cussen, E. J.; Vente, J. F.; Battle, P. D.; Gibb, T. C. *J. Mater. Chem.* **1997**, *7*, 459.

(28) Attfield, M. P.; Battle, P. D.; Bollen, S. K.; Gibb, T. C.; Whitehead, R. J. *J. Solid State Chem.* **1992**, *100*, 37.

(29) de la Calle, C.; Alonso, J. A.; García-Hernández, M.; Pomjakushin, V. *J. Solid State Chem.* **2006**, *179*, 1636.

(30) (a) Aguadero, A.; de la Calle, C.; Alonso, J. A.; Pérez-Coll, D.; Escudero, M. J.; Daza, L. *J. Power Sources* **2009**, *192*, 78. (b) Martínez-Lope, M. J.; Alonso, J. A.; Casais, M. T.; García-Hernández, M.; Pomjakushin, V. *J. Solid State Chem.* **2006**, *179*, 2506.

(31) Blasco, J.; Ritter, C.; Rodríguez-Velamazán, J. A.; Herrero-Martín, J. *Solid State Sci.* **2010**, *12*, 750.

(32) (a) Momin, A. C.; Mirza, E. B.; Mathews, M. D. *J. Mater. Sci. Lett.* **1991**, *10*, 1246. (b) Jiang, S. P. *J. Mater. Sci.* **2008**, *43*, 6799. (c) Yashima, M. In *Perovskite Oxide for Solid Oxide Fuel Cells*; Ishihara, T., Ed.; Springer: New York, 2009; pp 117−146.

(33) Kang, H.; Beauchamp, J. L. *J. Am. Chem. Soc.* **1986**, *108*, 5663.

(34) Carter, E. A.; Goddard, W. A., III *J. Phys. Chem.* **1988**, *92*, 2109.

(35) Heyd, J.; Scuseria, G. E.; Ernzerhof, M. *J. Chem. Phys.* **2006**, *124*, 219906.

(36) Kilner, J. A.; Berenov, A; Rossiny, J. In *Perovskite Oxide for Solid Oxide Fuel Cells*; Ishihara, T., Ed.; Springer: New York, 2009; pp 95−116.

(37) (a) Pavone, M.; Ritzmann, A. M.; Carter, E. A. *Energy Environ. Sci.* **2011**, *4*, 4933. (b) Lee, Y.-L.; Kleis, J.; Rossmeisl, J.; Morgan, D. *Phys. Rev. B* **2009**, *80*, 224101.

(38) (a) Nowotny, J.; Rekas, M. *J. Am. Ceram. Soc.* **1998**, *81*, 67. (b) Mizusaki, J.; Yoshihiro, M.; Yamauchi, S.; Fueki, K. *J. Solid State Chem.* **1985**, *58*, 257. (c) Mizusaki, J.; Mima, Y.; Yamauchi, S.; Fueki, K. *J. Solid State Chem.* **1989**, *80*, 102.

(39) Iwahara, H.; Esaka, T.; Mangahara, T. *J. Appl. Electrochem.* **1988**, *18*, 173.

(40) Jurado, J. R.; Fiqueiredo, F. M.; Gharbage, B.; Frade, J. R. *Solid State Ionics* **1999**, *118*, 89.

(41) Tao, S.; Canales-Vazquez, J.; Irvine, J. T. S. *Chem. Mater.* **2004**, *16*, 2309.

(42) Tuller, H. L. *Solid State Ionics* **1997**, *94*, 63.